Accepted Manuscript

Immobilized liquid metal nanoparticles with improved stability and photothermal performance for combinational therapy of tumor

Jing-Jing Hu, Miao-Deng Liu, Ying Chen, Fan Gao, Si-Yuan Peng, Bo-Ru Xie, Chu-Xin Li, Xuan Zeng, Xian-Zheng Zhang

PII: S0142-9612(19)30204-2

DOI: https://doi.org/10.1016/j.biomaterials.2019.03.043

Reference: JBMT 19154

To appear in: *Biomaterials*

Received Date: 22 January 2019

Revised Date: 16 March 2019

Accepted Date: 28 March 2019

Please cite this article as: Hu J-J, Liu M-D, Chen Y, Gao F, Peng S-Y, Xie B-R, Li C-X, Zeng X, Zhang X-Z, Immobilized liquid metal nanoparticles with improved stability and photothermal performance for combinational therapy of tumor, *Biomaterials* (2019), doi: https://doi.org/10.1016/j.biomaterials.2019.03.043.

Immobilized liquid metal nanoparticles with improved stability and photothermal performance for combinational therapy of tumor

Jing-Jing Hu,† Miao-Deng Liu,† Ying Chen, Fan Gao, Si-Yuan Peng, Bo-Ru Xie, Chu-Xin Li, Xuan Zeng,* Xian-Zheng Zhang*

Key Laboratory of Biomedical Polymers of Ministry of Education & Department of Chemistry, Wuhan University, Wuhan 430072, PR China

ABSTRACT

Various negative effects accompanying with the instability of bare liquid metal (LM) nanoparticles, including undesirable spontaneous coalescence, continuous photothermal performance deterioration and difficult multi-step functionalization, severely hinder its applications in biomedical area. In this study, we proposed a new concept of immobilized liquid metal nanoparticles based on a surface mesoporous silica coating strategy (LM@MSN). Strikingly, it was found that unsteady and vulnerable LM nanoparticles after immobilization exhibited enhanced stabilization and sustainable photothermal performance even with a long and repeated light irradiation in acidic environments. Moreover, integrating the properties of easy surface functionalization and high drug loading efficiency from silica shell, immobilized LM nanoparticle was further used for photothermal involved combinational therapy. The classical anticancer drug doxorubicin (DOX) was encapsulated in pores of silica shell and the hyaluronic acid (HA) was decorated on LM@MSN to construct LM@MSN/DOX@HA for tumor targeted combination therapy. Both *in vitro* and *in vivo* studies proved that LM@MSN/DOX@HA could significantly inhibit solid tumor growth under near infrared (NIR) irradiation by synergistic photothermal/chemotherapy.

Keywords: liquid metal, stabilization, mesoporous silica, combinational therapy, tumor.

† These authors contributed equally to this work.

* Corresponding authors. *E-mail addresses: xz-zhang@whu.edu.cn (X.Z.Z.), xuanzeng@whu.edu.cn (X.Z.).*

1. Introduction

Liquid metal (LM) gallium-indium eutectic alloy (75% Ga and 25% In), as a moldable, deformable and stretchable material, has attracted tremendous research interest in the world wide [1]. Its fascinating unique properties, such as large surface tension, excellent mobility, high electrical conductivity, good biocompatibility and low toxicity in contrast with mercury, indicate that LM is not only promising in the design of microfluidic systems, stretchable electronics and soft robotics [2-4], but also suitable for biomedical applications [5-9]. Nanoscale LM is facilely produced from bulk LM droplet via ultrasonication with the stabilizing effect of the natural surface oxide layer and surfactant thiolate ligands [10-13]. Very recently, the physicochemical properties of LM nanoparticles have been systemically explored by Miyako et al. [14] Outstanding photochemical and photothermal conversion properties of LM nanoparticle have been revealed initially, which is superior to many traditional photothermal conversion agents (PTAs), enabling its potential for PTT of tumor. Despite a few encouraging achievements, the development of LM nanoparticles for tumor therapy is still in its nascent stage [6, 7, 14-16].

It was found that LM nanoparticles had an enormous Achilles' heel-lack of stability, including colloidal stability, chemical stability as well as thermal stability, which could severely impede the broader applications, especially in PTT-involved tumor therapy. Specifically, the fluidity of LM could induce the irreversible aggregation and spontaneous coalescence of LM nanoparticles, and leading to the significant changes in the physicochemical properties and a detectable loss of activity. The acid in tumor tissue could react with both Ga and oxide of gallium into Ga(III) ions, which would induce undesirable and uncontrollable consumption of materials. What’s worse, under laser irradiation, produced heat could not only cause thermal expansion deformation, but also help to oxidize spherical LM nanoparticles to rodlike gallium oxide hydroxide (GaOOH) in aqueous solutions [17, 18], thus transforming their shape, accelerating deterioration, as well as losing photothermal conversion ability with prolonged irradiation period. As a promising PTA, thermal

instability of LM nanoparticles would dramatically restrict their sustainability and improvement of photothermal efficacy. On the other hand, it also brought some challenges with the multiple instabilities of LM nanoparticle, among which difficult nanoparticles' surface modification and functionalization is outstanding. At present, the surface decoration of LM nanoparticles mainly relies on the thiolate ligands and can hardly be multi-step and complex, which is not enough to satisfy diverse demands of therapy [10-13].

Here, for the first time, we proposed a concept of immobilized LM nanoparticles by a surface coating strategy to overcome the multiple instabilities and their concomitant problems. In this proof-of-concept study, a multifunctional mesoporous silica shell [19-21] was selected for the unstable and vulnerable LM nanoparticles (LM@MSN). As shown in Scheme 1, silica coating layer could not only ensure colloidal stabilization by preventing the aggregation and self-fusion of LM, but also thermal stabilization based on the rigid silica shell, which could fixate the shape, restrict the morphological changing of LM and reduce the exposure to the air and water to prevent the generation of GaOOH. Simultaneously, chemically inert silica shell could delay the contact of hydrogen ions and avoid early entry into the acid degradation stage before laser-triggered treatment, thus guaranteeing good photothermal conversion efficiency in PTT. More excitingly, compared with bare LM nanoparticles, which showed an obviously photothermal performance decay under repeated NIR irradiation, LM@MSN exhibited enhanced photothermal conversion efficiency and constant excellent photothermal performance even after repeated light irradiation in acidic environments. In addition, the coating of mesoporous silica could further endow the LM nanoparticles with easy surface functionalization, high drug loading efficiency, as well as controlled drug release by sophisticated molecular gatekeeper designs [22-27]. Then, the immobilized LM nanoparticle (LM@MSN) with enhanced stability and photothermal performance was further employed as a multifunctional nanoplatform for photothermal/chemotherapy (Scheme 1B). The classical anticancer drug doxorubicin (DOX) was encapsulated in the pores of MSN and then the hyaluronic acid (HA)

was further decorated on surface of LM@MSN to obtain LM@MSN/DOX@HA. HA was used as both a CD44-targeting functional polymer and enzyme-responsive gatekeeper for on demand drug release. After targeting to tumor, overexpressed hyaluronidase (HAase) in tumor tissue could trigger the DOX release for chemotherapy. Simultaneously, LM@MSN was excited to produce hyperthermia under light irradiation, thus achieving highly effective synergistic photothermal/chemotherapy. This integration of multifunctional mesoporous silica shell with LM exhibited great potential to immobilize LM, enhance stability and photothermal efficiency as well as provide sufficient drug loading and tumor targeting capability, thus significantly elevating the overall therapeutic performance.

2. Materials and methods

2.1. Materials

LM (Gallium Indium eutectic, 99.99%) was obtained from Alfa Aesar. Methoxypoly(ethylene glycol) thiol (mPEG-SH, Mw 5000) was purchased from Shanghai Ponsure Biotech, Inc. Hexadecyltrimethyl ammonium chloride (CTAC), teraethylorthosilicate (TEOS), triethanolamine (TEA) and triethylamine were purchased from Sinopharm Chemical Reagent Co., Ltd. 3-Aminopropyltriethoxysilane (APTES) and indocyanine green (ICG) were purchased from Aladdin Reagent Co. Ltd. (Shanghai, China). Doxorubicin hydrochloride (DOX·HCl) was obtained from Zhejiang Hisun Pharmaceutical Co., Ltd. (China). Hyaluronic acid (HA, 35 kDa) was purchased from Freda Biochem Co. Ltd. (Shandong, China). RPMI 1640 medium, trypsin, penicillin-streptomycin, fetal bovine serum (FBS), 3-[4,5-dimethylthiazol-2-yl-]-2,5 -diphenyltetrazolium-bromide (MTT) and Hoechst 33342 were purchased from Invitrogen Co. (United States). Calcein-AM, and propidium iodide (PI) were obtained from Sigma-Aldrich. All of the other reagents and solvents were provided by Sinopharm Chemical Reagent Co., Ltd.

2.2. Measurements

Transmission electron microscopy (TEM, Tecnai G2 20 TWIN) was used to study the morphology of nanoparticles. HADDF-STEM images and element mapping analysis were obtained on Tecnai G2 20 TWIN operated at 200 kV. Surface area was calculated by the Brunauer-Emmett-Teller (BET) approach and the pore size distributions were obtained by the Barret-Joyner-Halenda (BJH) method (ASAP2020, micromeritics). Fluorescence spectra were recorded on a RF-5301PC spectrofluorophotometer (Shimadzu). A Nano-ZS ZEN3600 particle sizer (Malvern Instruments) was used for zeta potential and hydrodynamic size of nanoparticles. UV-vis absorbance spectra of different samples were recorded by UV-vis spectrophotometer (Lambda Bio40, Perkin-Elmer). Confocal laser scanning microscopy (CLSM) imaging was conducted on a C1-Si (Nikon) confocal laser scanning microscope. The 808 nm NIR laser (STL808T1-7.0W, Beijing STONE Laser) was utilized to evaluate the photothermal conversion performance.

2.3. Preparation of LM nanoparticles

LM (700 mg) was added into the ethanol solution (15 mL) containing SH-mPEG (65 mg) and the mixture was sonicated in an ice-bath by a probe-type sonicator with a 6-mmφ probe at 80% intensity for 2 h (22 kHz, LC-1000, Ningbo Licheng Instrument Co., Ltd., Ningbo, China). After sonication, the larger nanoparticles were removed after centrifugation (1000rpm, 10min; 3000rpm, 10min; 5000rpm, 10min) in sequence. The solution was further centrifuged (12000rpm, 10min) to obtain LM nanoparticles. The results nanoparticles were washed with water for 3 times and stored in PBS buffer.

2.4. Preparation of LM@MSN

CTAC (2 g) was dissolved in deionized (DI) water (20 mL) under vigorously stirring at room temperature for 2 h. The LM nanoparticles (100 mg) were added to the CTAC solution and followed by stirring for another 1 h. Then TEOS (35 μL) was added to the mixture under vigorous stirring for 0.5 h at room temperature. The mixture was further added with TEA (100 μL) and stirred for 24 h at room temperature to acquire LM@MSN. 1wt% Solution of NaCl in methanol was used to remove the

template CTAC at room temperature. The resultant LM@MSN was washed with water for 5 times and ethanol for 5 times, respectively and stored in ethanol.

2.5. Preparation of LM@MSN-NH_2

LM@MSN (20 mg) was suspended in ethanol (50 mL) and then APTES (2 mL) was added to the solution under stirring for 24 h at 35 □. The obtained LM@MSN-NH_2 was centrifuged and washed with ethanol for 5 times and stored in ethanol.

2.6. Drug loading and preparation of LM@MSN/DOX@HA

DOX·HCl (4 mg) was dissolved in DMSO (4 mL) and then triethylamine (2 μL) was added into the solution under stirring for 12 h at room temperature in the dark to obtain a triethylamine-treated DOX. Then LM@MSN-NH_2 (20 mg) was further suspended in triethylamine-treated DOX solution and stirred for 12 h at room temperature in the dark. The LM@MSN/DOX was washed with water for several times to remove the excess DOX. Then the LM@MSN/DOX was dispersed in DI water and HA (50 mg/mL, 2 mL) was added to the solution. The mixture was further stirred for 12 h. The final LM@MSN/DOX@HA nanoparticles were washed with water for several times and stored in PBS buffer. For a comparison, LM@MSN@HA nanoparticles without drug loading were prepared under the same condition. Moreover, LM@MSN/ICG and LM@MSN/ICG@HA were prepared according to the similar methods.

2.7. In vitro photothermal performance

The LM@MSN suspended in PBS with concentrations from 0 to 10 μg/mL was irradiated by an 808 nm laser for 10 min with a power density of 1 W cm^{-2}. To study the influence of power density, the concentration of LM@MSN was fixed at 6 μg/mL and then irradiated by an 808 nm laser for 10 min with a power density of 0.25, 0.5, 1, 1.5 W cm^{-2}, respectively. To investigate the photothermal stability, LM or LM@MSN (with the same concentration of LM) was exposed to 808 nm laser (1 W cm^{-2}) for 10 min and following natural cooling process for five cycles. To investigate the stability in acidic conditions, LM or LM@MSN was dispersed in pH 7.4 or pH 5.0 solutions for 0 h, 12 h, 24 h.

Each solution was exposed to 808 nm laser for 10 min with a power density of 1 W cm^{-2}. The temperature variation was monitored by the FLIR Ax5 camera (FLIR Systems AB, Sweden).

2.8. Calculation of photothermal conversion efficiency

The photothermal conversion efficiency (η) of LM and LM@MSN was measured based on the reported methods [28-30]. The LM or LM@MSN (6 μg/mL) was irradiated by an 808 nm laser for 10 min with a power density of 1 W cm^{-2}.

The calculation was given as following:

$$\eta = [hs(T_{Max} - T_{Surr}) - Q_{Dis}]/I(1 - 10^{-A_{808}}) \quad (1)$$

h is the heat transfer coefficient, *s* is the surface area of the container, and the value of *hs* is obtained from the equation (4). The maximum steady temperature (T_{Max}) of the solution of the LM@MSN was 57.6 □ and LM was 50 □, while the environmental temperature (T_{Surr}) was 26.5 □. And Q_{Dis} expresses heat dissipated from the light absorbed by the plastic cell itself, and it was measured independently to be 10.2 mW using a dispersible plastic cuvette cell containing distilled water solvent and container.

The laser power *I* is 1.0 W·cm^{-2}. The absorbance of the LM and LM@MSN at 808 nm A_{808} is 0.4 and 0.31. In order to gain *hs*, a dimensionless parameter *θ* was introduced as followed:

$$\theta = (T - T_{Surr})/(T_{Max} - T_{Surr}) \quad (2)$$

A sample system time constant τ_s can be calculated as equation (2).

$$t = -\tau_s \ln(\theta) \quad (3)$$

According to Fig. 2F, S3, the τ_s of LM and LM@MSN were determined and calculated to be 283.76 s and 237.93 s. Then, *hs* can be calculated as equation (4):

$$hs = m_0 C_0/\tau_s \quad (4)$$

In addition, m_0 is 0.5 g and C_0 is 4.18 J·g^{-1}·□$^{-1}$. Thus, according to equation (4), *hs* of LM and LM@MSN were deduced to be 7.37 and 8.78 mW·□$^{-1}$.

Finally, the *η* of LM was deduced to be 27.1%, and the *η* of LM@MSN was 51.5%.

2.9. In vitro drug release study

To study the enzyme responsiveness of LM@MSN/DOX@HA, drug release profiles were conducted in following conditions: PBS; 0.15 mg/mL HAase; 0.3 mg/mL HAase and 0.6 mg/mL HAase. LM@MSN/DOX@HA was suspended in the above solution (3 mL) and incubated in 37 □, respectively. At given time intervals, the fluorescence intensity of the supernatant of incubation solution was measured by a Lambda Bio40 UV/vis spectrometer (Perkin-Elmer). And the nanoparticles were redispersed in fresh incubation solution.

2.10. Cell culture

Murine mammary carcinoma (4T1) cells were incubated in RPMI 1640 medium containing 10% FBS and 1% antibiotics (penicillin-streptomycin, 10000U mL^{-1}) at 37 □ in a humidified atmosphere containing 5% CO_2.

2.11. Study the tumor-targeted uptake of LM@MSN/DOX@HA by CLSM and ICP-AES Assay

4T1 cells were seeded in the glass bottom dishes at a density of 1×10^5 cells per well for 1 day. One well of 4T1 cells was pre-incubated with free HA (2 mg/mL) for 4 h. Then the cells were incubated with LM@MSN/DOX@HA (containing 6 μg/mL Ga) for 2 h, 4 h or 8 h, respectively. As to the control groups of COS7 cells, LM@MSN/DOX@HA was incubated in the same conditions. Afterward, the media were removed and the cells were washed with PBS to remove the extracellular nanoparticles. The cells were incubated with Hoechst 33342 at 37 ℃ for 15 min to stain the cellular nuclei. Finally, all the cells were visualized by CLSM (Nikon C1-si, Japan). Moreover, 4T1 cells were seeded onto 6-well plates at a density of 5×10^5 cells and grew for 1 day. Then the cells were incubated with LM@MSN@HA or LM@MSN (both containing 6 μg/mL Ga) for 2 h, 4 h or 8 h, respectively. After being washed by PBS, the cells were digested by trypsin and collected through centrifugation. To measure the cellular Ga content, the cells were digested by aqua regia (extreme caution is required! Aqua regia is highly corrosive and damaging to skin and eyes!). The solution

was diluted with DI water to 10 mL. Ga content was examined based on ICP-AES analysis (IRIS Intrepid II XSP).

2.12. Live/dead cell staining assay

To evaluate cell injury after exposure to NIR, 4T1 cells were seeded in 24-well plates at a density of 1×10^5 cells per well and grew for 24 h. The cells were treated with PBS, LM@MSN, LM@MSN@HA, LM@MSN/DOX@HA (both containing 6 μg/mL Ga) for 4 h, respectively. Then the cells were replaced by fresh medium and the illumination groups were irradiated by 808 nm laser for 5 min (1.0 W cm^{-2}). After further incubation for 12 h, each sample was incubated with calcein-AM (4 μM) and PI solutions (4 μM) in PBS buffer solution for 15 min at 37 ℃. At last, the cells were washed with PBS and observed by inverted fluorescence microscope (Olympus IX73).

2.13. In vitro cytotoxicity study

The cytotoxicity of LM@MSN@HA under different irradiation time and power density was estimated in 4T1 cells by MTT assay. 4T1 cells were seeded in the 96-well plates at a density of 6000 cells per well for 1 day. The cells were co-incubated with LM@MSN@HA (containing 0.6 μg/mL Ga) for 4 h and irradiated by 808 nm laser for different times (3 min) or at different power density (1.0 W cm^{-2}). After further incubation for 24 h, MTT (5 mg/mL, 20 μL) was added to each well and incubated for another 4 h. Afterward, the medium was replaced with DMSO (150 μL). The absorbance at 570 nm was measured by a microplate reader (Bio-Rad, Model 550, USA). The relative cell viability was calculated according to the following equation: cell viability= $(OD_{570(samples)}/OD_{570(control)})\times100\%$, where $OD_{570(samples)}$ was obtained with treatment in the presence of nanoparticles and $OD_{570(control)}$ was obtained without treatment. To evaluate the enhanced cytotoxicity of combinational therapy, 4T1 cells were seeded in the 96-well plates at a density of 6000 cells per well for 1 day. The cells were co-incubated with LM@MSN@HA or LM@MSN/DOX@HA at different concentrations for 4 h and the illumination groups were irradiated by 808 nm laser for 5 min (1.0 W cm^{-2}). The cells were further incubated for 24 h. The following

process was the same. To evaluate the cytotoxicity of LM@MSN@HA, 4T1 cells, HeLa cells, MCF-7 cells and 3T3 cells were seeded in the 96-well plates at a density of 6000 cells per well for 1 day, respectively. The cells were co-incubated with LM@MSN@HA at different concentrations for 24 h. The following process was the same.

2.14. Animal tumor xenograft models

BALB/c mice (4-week old, female) were bought from Wuhan University Animal Biosafty Level III Lab. All study protocols were approved by the Institutional Animal Care and Use Committee (IACUC) of the Animal Experiment Center of Wuhan University (Wuhan, China). All mouse experimental procedures were performed in accordance with the Regulations for the Administration of Affairs Concerning Experimental Animals approved by the State Council of People's Republic of China. To establish the 4T1 xenograft models, 4T1 cells (1×10^6 per mouse) were injected subcutaneously into right hind flank of the mice.

2.15. .In vivo fluorescence imaging and biodistribution

When the tumor volume reached 150 mm^3, mice were injected with LM@MSN/ICG or LM@MSN/ICG@HA (Ga concentration at 150 μg/mL, 100 μL) intravenously, respectively. Then the mice were anesthetized and imaged by the IVIS Spectrum (PerkinElmer) at 1 h, 3 h, 5 h, 9 h, 12 h, 24 h, 36 h after injection. After 36 h post-injection, the mice were sacrificed and the major organs (heart, liver, spleen, lung and kidney) and tumor tissues were dissected for imaging.

2.16. In vivo tumor photothermal imaging

When the tumor volume reached 150 mm^3, mice were injected with LM@MSN or LM@MSN@HA (Ga concentration at 150 μg/mL, 100 μL) intravenously, respectively. The mice injected with PBS buffer were utilized as the control. Infrared thermal images were recorded by a FLIR Ax5 camera with NIR irradiation (808 nm, 1 W cm^{-2}, 5 min).

2.17. In vivo antitumor study and histochemistry analysis.

When the tumor volume reached 100 mm^3, 4T1 tumor-bearing mice were divided into 5 groups randomly (n≥5) and treated with (1) PBS, (2) LM@MSN@HA, (3) LM@MSN/DOX@HA, (4) LM@MSN@HA+NIR and (5) LM@MSN/DOX@HA +NIR (fixed Ga concentration at 150 μg/mL, 100 μL). The light groups were irradiated by 808 nm laser (1.0 W cm^{-2}) for 5 min after injection for 24 h. And tumor volumes and body weights of mice in five groups were monitored every day. Tumor volume was measured by calipers. Tumor volume= tumor length × tumor $width^2/2$. All the mice were euthanized after 14-day treatment. Main organs (heart, liver, spleen, lung and kidney) and tumors were dissected, washed and used for histology analysis, TUNEL immunofluorescence staining and immunofluorescence staining of caspase 3.

2.18. Excretion study.

The mice were injected with LM nanoparticles, intravenously and housed in metabolic cages. The urine and feces were collected at different time points and digested by aqua regia. The solution was diluted with DI water to 10 mL. Ga content was examined based on ICP-AES analysis (IRIS Intrepid II XSP).

3. Results and discussion

3.1. Design, preparation and characterization of immobilized LM nanoparticles

A schematic illustration of the preparation of bare LM nanoparticles and immobilized LM nanoparticles were shown in Fig. 1A. In this study, with several optimizations to previous reports [10-13], we obtained relatively stable LM nanoparticles by probe sonication in ethanol solution with methoxypoly(ethylene glycol) thiol (mPEG-SH). The role of indispensable mPEG-SH was not just to stabilize the LM nanoparticles and prevent spontaneous coalescence but also to contribute to the condensation of silica on the surface of LMs considering the affinity of PEG toward silica [31]. After sonication in ice bath, gradient centrifugation was further used to obtain the uniform LM nanoparticles from a broad size distribution of nanoparticles. As shown in Fig. S1 and 1B,

reddish-brown LM solution was produced and transmission electron microscopy (TEM) image proved that well-distributed and uniform LM was prepared successfully. The hydrodynamic size of LM characterized by dynamic light scattering (DLS) was 81.94 nm (PDI=0.135) (Table S1). It's worth mentioning that the bare LM nanoparticles cannot be long-term preservation, which would tend to irreversible aggregate and self-fuse after prolonged storage time (Fig. S2).

In the second step, the mesoporous silica shell was chosen to functionalize the bare LM nanoparticles. Despite the mature technology and great advancements in SiO_2 coated nanomaterials, the classic silica coating based on the well-known base catalyzed co-condensation methods is very challenging to LMs owing to the easy fusion and transformation of unstable LMs under higher temperature, as well as the property to react with both base and acid, which is essential in catalyzing teraethylorthosilicate (TEOS) hydrolysis and removing the surfactant template in the pores of silica layer, respectively. In this case, the mesoporous silica coating procedures and conditions should be controlled precisely, otherwise frustrating coating may appear. As shown in Fig. 1C, the thickness of the silica shell could effectively be tuned by varying the silica source (TEOS) concentrations. With the increasing of TEOS, shell would thicken, which could provide more sufficient drug loading space. However, excess TEOS might also produce random SiO_2 core without modification on liquid metal as displayed in Fig. $1C_4$, which is hard to be purified. To obtain the uniform LM@MSN with satisfying drug loading efficiency, monodispersed core-shell LM@MSN in Fig.$1C_3$ was selected to conduct the following investigation and the optimal Si thickness was about 15 nm. The digital picture of LM@MSN in phosphate buffered saline (PBS) (Fig. S1) demonstrated that their excellent dispersity and hydrophilicity after silica coating. The hydrodynamic size of LM@MSN increased to 127.1 nm (PDI=0.14) (Table S1). In addition, the disappointing thermal stability of bare LM nanoparticles required the good control of the temperature during whole preparation processes, if not, the re-shaping of LM might occur (Fig. S3). The chemical instability of LM requested the reasonable TEA concentrations and introduction time to accelerate the TEOS hydrolysis and reduce the

consumption of LM (Fig. $1D_1$, $1D_2$). The multiple LM nanoparticles would be coated by a whole silica shell under low stirring rate (Fig. $1D_3$). As shown in Fig. 1E, after being etched by hydrochloric acid, the hollow SiO_2 shell could better prove the successful coating of silica. Moreover, the high-angle annular dark field scanning transmission electron microscopy (HAADF-STEM) images and element mapping of LM@MSN confirmed that gallium and indium were presented in the core of the nanoparticle, while silica and oxygen appeared in the out shell as expected (Fig. 1F). In addition, the zeta potential of LM@MSN decreased significantly from positively charge of LM (27.3 mV) to negatively charge (-29.0 mV) (Table S2). These results indicated that the mesoporous SiO_2 shell could grow on the surface of LM nanoparticles successfully.

3.2. Improved photothermal performance of immobilized LM nanoparticles

As an excellent photothermal conversion agent (PTA), some conditions must be fulfilled: A) high photothermal conversion ability; B) superior photothermal stability; C) good biocompatibility and nontoxic [32-34]. As shown in Fig. 2A, both the LMs and LM@MSNs displayed a broad absorption band from the ultraviolet (UV) to near-infrared (NIR) regions, which was consistent with previous published LM colloidal solutions.[14] The obvious absorbance at NIR region could be observed, which was matched well with the 808 nm laser used in PTT and the silica coating did not significantly weaken the absorbance. The mass extinction coefficient of LM@MSN at 808 nm was calculated to be 32.3 $Lg^{-1}cm^{-1}$, which was much higher than that of other common PTAs, such as Au nanorods (13.9 $Lg^{-1}cm^{-1}$) [35], graphene oxide (3.6 $Lg^{-1}cm^{-1}$), reduced GO (rGO) (24.6 $Lg^{-1}cm^{-1}$) [35], WS_2 nanosheet (23.8 $Lg^{-1}cm^{-1}$)[36] and MoS_2 (28.4 $Lg^{-1}cm^{-1}$) [37]. Next, LM and LM@MSN were irradiated by an 808 nm laser for 10 min to systematically investigate their photothermal conversion property (Fig. 2). The temperature elevation curve monitored by an IR camera indicated that the presence of LM could rapidly and efficiently generate heat from photo energy. Besides, the temperature rising speed and ultimate temperature were positively associated with the concentration of nanoparticles (Fig. 2B) and power density (Fig. 2C), demonstrating that the increased temperature

could be precisely controlled. Moreover, photothermal heating curves of LM with larger hydrodynamic sizes by different centrifugal force was provided, indicating the size of LM nanoparticles actually has some effect on photothermal conversion ability as reference (Fig. S4). The photothermal performance of LM@MSN with a thicker silica shell (~25 nm) was also measured in the same conditions. The results demonstrated that the silica thickness within certain limits had little effect on photothermal conversion ability as shown in Fig. S5. Interestingly, we noticed that the LM before and after silica coating at same concentration exhibited a similar temperature increasing rate under the initial irradiation, and subsequently, the LM@MSN could induce more significant temperature elevation compared to bare LM without protective shell (Fig. 2D). In addition, an important parameter photothermal conversion efficiency (η) to evaluate the photothermal conversion ability of PTAs was calculated according to a published method [28-30]. The photothermal conversion efficiency (η) of LM@MSN increased to 51.5% (Fig. 2E, 2F), which was significantly higher than most of PTAs in the literature, like gold-based nanostructures, 2D inorganic photothermal agents (summarized in Table S3). In contrast, the photothermal conversion efficiency (η) of LM was measured to be 28.3% of 808 nm (Fig. 2G, 2H), further proving that the importance of silica coating to promote the photothermal performance of LM. It's worth noting that though LM@MSN exhibited a better photothermal performance, LM will lose the fluid and degradable properties to some extent after immobilized by mesoporous silica.

Next, the photothermal stability of nanoparticles was also investigated. The temperature change of LM and LM@MSN were recorded under irradiation by 808 nm laser for 10 min and following natural cooling process for five cycles. As displayed in Fig. 2I and 2J, the maximal temperature of LM during each cycle showed a significant decline from 50 □ to 43.2 □, demonstrating the disappointing thermal stability, which would severely limit its future development. The photothermal conversion efficiency (η) of LM@MSN was the same under second light irradiation. However, the photothermal conversion efficiency (η) of bare LM further declined to 17.9% of 808 nm under

second light irradiation (Fig. 2K). To further confirm the photothermal performance of completely transformed LM, LM nanoparticles solution was heated at 70 □ for 2 h according to a previous report [18]. As shown in Fig. S6, the completely transformed LM that included gallium oxide hydroxide had not photothermal conversion ability. Excitingly, LM after protected by silica shell could not only guarantee higher photothermal conversion efficiency but also exhibit excellent temperature rising capability under repeated NIR laser switch-on/off, clearly demonstrating that the silica coating could overcome the fatal flaw of LM as a PTA for PTT and promote it to a durable PTA, which was a qualitative leap on the property of materials.

3.3. Improved thermal stability of immobilized LM nanoparticles

To detailed study the influence of silica layer on the LMs thermal stability, the morphology change of LM and LM@MSN after 808 nm laser irradiation for 10 min was visualized by TEM. Compared to the uniform and spherical nanoparticles before irradiation, LM under NIR treatment collapsed and transformed to spindle-like nanoparticles (Fig. 3B), which was the same as previous literatures and proved to be spindle-like gallium oxide hydroxide (GaOOH) [15,16]. The TEM image of LM after NIR irradiation for 5 cycles was also provided (Fig. S7). There is no noticeable difference between the TEM images of LM after NIR treatment between one cycle and five cycles. In contrast, LM@MSN was basically unchanged and remained a remarkable core-shell structure (Fig. 3C). These results matched well with the significant increase in hydrodynamic diameter and size distribution of LM after laser irradiation examined by DLS (Fig. 3D), while those of LM@MSN did not change, confirming their better stability (Fig. 3E, 3F). Furthermore, the optical properties were also measured. As displayed in digital pictures (Fig. 3G), the LM@MSN solution kept the original color very well compared to the lighter color of bare LM solutions after irradiation. The corresponding absorption spectra of bare LM solutions illustrated that the absorbance intensity diminished significantly with NIR excitation (Fig. 3H). In comparison, the LM@MSN was more stable as presented in Fig. 3I and the absorbance intensity remained approximately constant. We

hypothesized that the LM could degrade in water upon NIR light owing to the generated heat, which could not only cause thermal expansion deformation, but also help to oxidize spherical nanoparticles to rodlike GaOOH in aqueous solutions, followed by conversion to the final Ga(III) ions. Therefore, the decrease in absorbance was caused by the degradation of the bare LM. In comparison, the LM@MSN exhibited stronger absorption than the LM attributed to coating of silica shell. The hard material SiO_2 could fixate the shape, restrict the morphological changing to some extent and reduce the exposure to the air and water, to prevent the generation of GaOOH, endowing the LM with enhanced stability even under the light-induced heat. These results above clearly illustrated that the LM@MSN exhibited a superior thermal stability after protecting by silica shell.

3.4 Enhanced chemical stability of immobilized LM nanoparticles in acidic environments

As we all known, tumor acidic microenvironment is a non-negligible condition. Both Ga and oxide of gallium could react with acid and then degrade into Ga(III) ions. This acid degradation reaction could also be facilitated under the produced heat. To avoid early entry into the acid degradation stage before getting adequate laser-triggered treatments, PTAs should be relatively stable in tumor tissues to ensure a good effect of treatment. Toward this end, we further investigated the impact of silica shell on the deterioration behavior of LM in acidic conditions (Fig. 4A). The LM and LM@MSN were incubated with the phosphate-buffered saline (PBS, pH 7.4) and acidic solution (pH 5.0) at 25 □, respectively (Fig. 4B). Compared to the changeless LM in PBS, the color of LM in acid solutions was getting lighter and lighter with the increasing incubation time, proving the acid-triggered degradation behavior of LM. In comparison, the LM@MSN could maintain the color well both in neutral or acidic conditions. Further, the residual LM amount during the degradation process was measured based on the absorption of LM. It was found that in LM with pH 5.0, a degradation ratio of nearly 30% was displayed during the initial 6 h and a significant sustained downward trend was shown until 36 h, but LM@MSN could be quite stable after silica coating even in acidic conditions (Fig. 4C). Moreover, the photothermal performance of LM and LM@MSN

under different pH values was assessed, respectively (Fig. 4D, 4E). After 808 nm laser irradiation, the temperature rise of LM in acidic solution was 35 □ at initial stage, but after 12 h, the temperature increased by only 10 □ because of the LM deterioration. In contrast, after 12 h, the heat produced capability of LM@MSN was very close to the initial state both in neutral or acidic solutions. It further demonstrated that the important role of silica shell, which could efficiently inhibit the degradation of LM and retain the photothermal property before getting adequate treatment. It was worth noting that a small downward trend was observed from LM@MSN after incubation in acidic solutions for 24 h, suggesting that the mesoporous silica could not completely prevent the deterioration but delay the contact of hydrogen ions, which was beneficial for biodegradability. Moreover, the photothermal stability of LM@MSN in acidic solution was also studied and results proved the excellent temperature rising capability of LM@MSN under repeated NIR laser switch-on/off in acidic conditions (Fig. 4F).

3.5 Synthesis and characterization of LM@MSN/DOX@HA

The immobilized LM nanoparticle (LM@MSN) with enhanced stability and photothermal performance is further used as a multifunctional nanoplatform for photothermal/chemotherapy. The continuous modification process was monitored by the variations in zeta potential (Fig. 5B) and X-ray photoelectron spectroscopy (XPS) (Fig. S8). After prepared LM@MSN successfully, the nanoparticles was modified with 3-aminopropyltriethoxysilane (APTES) to construct LM@MSN-NH2. The zeta potential of LM@MSN-NH2 elevated obviously to a positively charge (30.9 mV) from negatively charge of LM@MSN, confirming successful anchor of amine groups. Subsequently, the classical anticancer drug doxorubicin (DOX) was encapsulated into the pores of LM@MSNs after vigorously stirring the mixture solution. Lastly, the resultant nanoparticle was decorated with hyaluronic acid (HA) as both a CD44-targeting functional polymer and enzyme-responsive gatekeeper for on demand drug release via electrostatic adsorption, leading to the negatively charged LM@MSN/DOX@HA (-22.4 mV). After drug loading and surface modification,

the hydrodynamic diameter of nanoparticles increased to 160.4 nm (PDI=0.089) and maintained the monodisperse distribution (Fig. 5C), the mesostructure of LM@MSN/DOX@HA in TEM image was unclear and fuzzy (Fig. 5D). Further, the hydrodynamic diameter changes of LM@MSN/DOX@HA in PBS and PBS with 10% serum were negligible during 36 h incubation, proving the well stability of LM@MSN/DOX@HA under physiological condition (Fig. S9). Besides, as examined by the RF-5301PC spectrofluorophotometer, the drug loading efficiency (DLE) of LM@MSN/DOX@HA was 5.1%. The enzyme-responsive drug release profiles of DOX from LM@MSN/DOX@HA were assessed. As shown in Fig. 5E, without adding HAase, LM@MSN/DOX@HA was gated by HA effectively and less than 20% of DOX was leaked after 36 h incubation. In contrast, more than 70% DOX was released after the incubation with 0.6 mg/mL HAase for 36 h, demonstrating that the HA coating could realize the enzyme-responsive DOX release in tumor tissue.

To test the tumor-targeting capability of LM@MSN/DOX@HA, CD44 positive cell lines (4T1 (murine mammary carcinoma cells)) and CD44 negative normal cell lines (COS7 (kidney fibroblast cell)) were utilized. As displayed in Fig. 5F, obvious red fluorescence of DOX was found in 4T1 cells, and the intensity of fluorescence became stronger after prolonging the incubation time. For comparison, weak red fluorescence was detected in COS7 cells, even with increasing the incubation time. Further, weak red fluorescence was also found in 4T1 cells, where excess free HA was added to block the CD44 receptor before co-incubation with LM@MSN/DOX@HA (Fig. S10). This was attributed to the HA on nanoparticles to selectively bind to overexpressed CD44 receptors on 4T1 cells. Moreover, intracellular gallium content detected by ICP-AES also confirmed the tumor-targeting capacity of LM@MSN/DOX@HA (Fig. S11). Compared to the nontargeted nanoparticles, the intracellular gallium content of LM@MSN@HA in 4T1 cells was 2.55-fold, 2.99-fold higher than that of LM@MSN without HA coating for 2 h and 4 h, respectively. These results demonstrated that LM@MSN/DOX@HA could be selectively uptaken by tumor cells and reduce the adverse effects to normal cells.

3.6 Evaluation cytotoxicity in vitro of LM@MSN/DOX@HA.

The phototoxicity of LM@MSN@HA was analyzed by methylthiazolyl tetrazolium (MTT) assay in vitro. Firstly, the cell viability of blank LM@MSN@HA was evaluated. The viabilities of LM@MSN@HA in both tumor cells (4T1, HeLa, MCF-7) and normal cells (3T3) were higher than 80%, even at a relatively high concentration (Fig. S12), displaying low toxicity and good biocompatibility of nanoplatfroms. After co-incubation with LM@MSN@HA for 4 h, the 4T1 cells were illuminated by 808 nm laser with different power density and time periods. The cell viability was measured after co-incubation for 24 h. The phototoxicity of LM@MSN@HA enhanced remarkably with increasing irradiation time and power density (Fig. 6A, 6B). The cell survival ratio was about 50% for 3 min irradiation, and decreased to only 3% for 5 min irradiation, demonstrating the excellent photothermal therapeutic effect. Next, the synergistic effect of PTT and chemotherapy for killing tumor cells by LM@MSN/DOX@HA was detected in 4T1 cells. As shown in Fig. 6C, in comparison with LM@MSN@HA treated 4T1 cells, there was a moderate increase in cell toxicity that treated with LM@MSN/DOX@HA owing to the anticancer drug DOX released from nanoparticles. After 808 nm laser irradiation, more 4T1 cells treated with LM@MSN@HA were killed via photothermal therapy. LM@MSN/DOX@HA showed remarkable cytotoxicity under NIR irradiation, ascribing to the synergistic effect of PTT and chemotherapy (Fig. 6D). Meanwhile, fluorescence live/dead cell assay was also used to direct observe the synergistic effect of LM@MSN/DOX@HA under NIR irradiation (Fig. 6E). The results had a similar tendency with MTT assay and demonstrated that when LM@MSN or LM@MSN@HA was incubated in 4T1 cells and not received light irradiation, only green fluorescence could be observed. When cells were exposed by light irradiation, almost all 4T1 cells still kept alive in LM@MSN group, owing to the limited uptaken amount in 4 h without HA assist. Obvious red fluorescence was observed when the cells were treated with LM@MSN@HA under laser irradiation or LM@MSN/DOX@HA, indicating that both the hyperthermia caused by LM@MSN@HA and chemotherapy mediated by DOX

released form LM@MSN/DOX@HA could induce cell death. Almost all 4T1 cells treated with LM@MSN/DOX@HA exhibited strong red fluorescence, suggesting the high tumor kill efficacy of combinational treatments.

3.7. In vivo biodistribution and photothermal conversion assay.

To evaluate the in vivo tumor-targeting capability of LM@MSN@HA, NIR dye indocyanine green (ICG) was encapsulated in nanosystems (LM@MSN/ICG and LM@MSN/ICG@HA) for in vivo fluorescence imaging. LM@MSN/ICG and LM@MSN/ICG@HA were injected into 4T1 bearing mice intravenously, respectively. Fig. S13A demonstrated that both two nanoparticles could accumulate in tumor obviously after injection and have relative long-time tumor retention. As expected, LM@MSN/ICG@HA with tumor targeting ability had better tumor accumulation efficiency than LM@MSN/ICG. After treatment for 36 h, the ex vivo fluorescence imaging results demonstrated that the fluorescence intensity in tumor tissue was higher than that in heart, spleen, kidney measured by semiquantitative mean fluorescence intensity (MFI) analysis (Fig. S13), which was consistent with the biodistribution results determined by ICP-AES (Fig. S14).

To further confirm the photothermal conversion capability of LM@MSN *in vivo*, 4T1 bearing mice were intravenously injected with LM@MSN and LM@MSN@HA, respectively and the temperature change was recorded every 30 s. As shown in Fig. 7A, with NIR laser exposure, the local temperature of tumor tissue in LM@MSN@HA group increased sharply and reached ~ 46.5 □ after 1 min irradiation. The final local tumor temperature reached ~ 54.2 □ after 5 min irradiation, which was high enough to thermally ablate tumor cells in vivo. For comparison, LM@MSN group had slower temperature increase rate and the ultimate temperature was just ~41.5 □ that was below the threshold temperature to kill cells. As to PBS group, the tumor temperature change was not obvious and about 5 □ under the same irradiation conditions (Fig. 7B). Therefore, LM@MSN@HA with HA assist could accumulate in tumor tissue efficiently, realize photothermal conversion under 808 nm exposure, lead to local hyperthermia.

3.8. Antitumor experiments in vivo.

Encouraged by the satisfactory therapeutic effect in vitro and the favorable NIR-induced hyperthermia in vivo, LM@MSN/DOX@HA was further investigated in antitumor study in vivo. The 4T1 tumor-bearing mice were divided into five experimental groups randomly ($n \geq 5$) and treated with (1) PBS, (2) LM@MSN@HA, (3) LM@MSN/DOX@HA, (4) LM@MSN@HA+NIR and (5) LM@MSN/DOX@HA +NIR. The light groups were irradiated by 808 nm laser (1.0 w/cm^2) for 5 min after injection for 24 h. Body weight of all mice was recorded every day and no obvious variation was observed in all five groups, demonstrating the well biocompatibility of designed nanoplatforms (Fig. 8A). As shown in Fig. 8B, the volume of PBS-treated tumor increased sharply and reached about 8-fold of the initial volume after 14-day treatment. Similarly, without NIR irradiation, LM@MSN@HA could not inhibit tumor growth and grew to 7.3-fold of the initial volume. Moreover, the LM@MSN/DOX@HA-treated tumor could be inhibited to some extent, ascribing to the DOX released from the LM@MSN/DOX@HA. Compared to the single hyperthermia treatment mediated by LM@MSN@HA, by integration of chemotherapy and PTT, LM@MSN/DOX@HA could suppress the tumor growth significantly, suggesting the superiority of LM@MSN/DOX@HA under NIR irradiation in maximizing the antitumor efficacy. After 14 days treatment, mice were euthanized and the tumors were collected. Both average tumor weight (Fig. 8C) and the corresponding tumor photos (Fig. 8D) were provided to demonstrate preferable therapeutic outcome of LM@MSN/DOX@HA under NIR laser irradiation compared to chemotherapy or PTT alone. Moreover, hematoxylin and eosin (H&E) staining of tumor tissues was employed to confirm the optimal antitumor capability of LM@MSN/DOX@HA under NIR laser irradiation. As displayed in Fig. 8E, in contrast with abundant tumor cells in PBS or LM@MSN@HA group, and limited destroyed tumor cells in LM@MSN/DOX@HA or LM@MSN@HA+NIR group, the tumor cells in LM@MSN/DOX@HA+NIR group exhibited more cell shrinkage and nuclei absence, indicating obvious cell damage. The therapeutic process was evaluated by the terminal deoxynucleotidyl

transferase (TdT)-mediated dUTP nick end labeling (TUNEL) assay (Fig. 8F). Compared to other treatment groups, the maximum amount of apoptotic cells was detected in the LM@MSN/DOX@HA+NIR group. In addition, immunofluorescence staining results showed that caspase 3 (red fluorescence) (Fig. 8G) was up-regulated after individual therapeutic treatment and markedly up-regulated under combinational treatment. Collectively, these results above confirmed that LM@MSN/DOX@HA+NIR integrated chemotherapy with PTT demonstrated superior efficiency in suppressing tumors.

In the meantime, the biosafety was also estimated. H&E images of major organs demonstrated that the low systemic toxicity of nanosystem, since no obviously pathological abnormalities in the heart, liver, spleen, lung, and kidney were found after different treatments (Fig. S15). To further study the excretion of LM nanoparticles *in vivo*, the fate of Ga element from excrement was monitored after *i.v.* injection. The results demonstrated that the LM could be excreted out efficiently through urine and feces over time (Fig. S16). Additionally, haematological assessment and blood biochemistry assay were used to evaluate the toxicology of designed nanosystem. The levels of important hematological parameters (Table S4) and the blood biochemical parameters (Table S5) were all within normal ranges, demonstrating that LM@MSN/DOX@HA presented negligible systemic side effects and had great potential in biomedical fields.

3. Conclusions

In summary, a multifunctional mesoporous silica shell was designed for the unstable and vulnerable LM nanoparticles. It was found that the silica coating layer could not only ensure LM nanoparticles' colloidal stabilization, chemical stabilization, but also thermal stabilization. Moreover, compared to the serious photothermal performance decay observed from the bare LM nanoparticles, the LM nanoparticles after immobilization exhibits extraordinary photothermal conversion efficiency and constant photothermal performance even after a long period and repeated light irradiation. Both in vitro and in vivo studies proved that after loading DOX and capped by HA,

LM@MSN/DOX@HA could realize tumor-targeted combinational therapy and significantly inhibit the solid tumor growth under NIR irradiation. As the first example of protecting and functionalizing bare LM nanoparticles, this study established LM@MSN as a promising nanoplatform for enhanced PTT-involved combinational tumor therapy.

Appendix A. Supplementary data

Supplementary data associated with this article can be found online at http:// xxxxxxxxxxx

Acknowledgements

This work was supported by the National Natural Science Foundation of China (51873162, 51833007 and 51690152). The authors would like to thank Pei Zhang and An-Na Du from The Core Facility and Technical Support, Wuhan Institute of Virology, for their help with producing TEM micrographs.

Disclosure of conflicts of interest

The authors declare no competing financial interests.

Data availability

The raw/processed data required to reproduce these findings are available from the authors.

References

[1] J. Liu, L. Yi, Liquid Metal Biomaterials: Principles and Applications, Springer Nature Singapore Pte Ltd, 2018.

[2] D. Wang, C. Gao, W. Wang, M. Sun, B. Guo, H. Xie, et al., Shape-Transformable, Fusible Rodlike Swimming Liquid Metal Nanomachine, ACS Nano 12 (2018) 10212-10220.

[3] N. Kazem, T. Hellebrekers, C. Majidi, Soft Multifunctional Composites and Emulsions with Liquid Metals. Adv. Mater. 29 (2017) 1605985.

[4] A. Chiolerio, M. B. Quadrelli, Smart Fluid Systems: The Advent of Autonomous Liquid Robotics. Adv. Sci. 4 (2017) 1700036.

[5] J. Yan, Y. Lu, G. Chen, M. Yang, Z. Gu, Advances in Liquid Metals for Biomedical Applications. Chem. Soc. Rev. 47 (2018) 2518-2533.

[6] L. T. Yi, J. Liu, Liquid Metal Biomaterials: A Newly Emerging Area to Tackle Modern Biomedical Challenges. Int. Mater. Rev. 62 (2017) 415-440.

[7] Y. Lu, Y. Lin, Z. Chen, Q. Hu, Y. Liu, S. Yu, et al., Enhanced Endosomal Escape by Light-Fueled Liquid-Metal Transformer. Nano Lett. 17 (2017) 2138-2145.

[8] Y. Lu, Q. Hu, Y. Lin, D. B. Pacardo, C. Wang, W. Sun, et al., Transformable Liquid-Metal Nanomedicine. Nat. Commun. 6 (2015) 10066.

[9] Y. Yu, E. Miyako, Manipulation of Biomolecule-Modified Liquid-Metal Blobs. Angew. Chem. Int. Ed. 56 (2017) 13606-13611.

[10] L. Ren, J. Zhuang, G. Casillas, H. Feng, Y. Liu, X. Xu, et al., Nanodroplets for Stretchable Superconducting Circuits. Adv. Funct. Mater. 26 (2016) 8111-8118.

[11] Y. Lin, C. Cooper, M. Wang, J. J. Adams, J. Genzer, M. D. Dickey, Handwritten, Soft Circuit Boards and Antennas Using Liquid Metal Nanoparticles. Small 11 (2015) 6397-6403.

[12] J. N. Hohman, M. Kim, G. A. Wadsworth, H. R. Bednar, J. Jiang, M. A. LeThai, et al., Nano Lett. 11 (2011) 5104.

[13] S. Sudo, S. Nagata, K. Kokado, K. Sada, Direct Synthesis of Liquid Metal Colloids and Their Transmetalation into Noble Metal Nanoparticles. Chem. Lett. 43 (2014) 1207-1209.

[14] S. A. Chechetka, Y. Yu, X. Zhen, M. Pramanik, K. Pu, E. Miyako, Light-Driven Liquid Metal Nanotransformers for Biomedical Theranostics. Nat. Commun. 8 (2017) 15432.

[15] X. Wang, W. Yao, R. Guo, X. Yang, J. Tang, J. Zhang, et al., Soft and Moldable Mg-Doped Liquid Metal for Conformable Skin Tumor Photothermal Therapy. Adv. Health. Mat. 7 (2018) 1800318.

[16] X. Sun, M. Sun, M. Liu, B. Yuan, W. Gao, W. Rao, et al., Shape Tunable Gallium Nanorods Mediated Tumor Enhanced Ablation Through Near-Infrared Photothermal Therapy. Nanoscale 11 (2019) 2655-2667.

[17] C. C. Huang, C. S. Yeh, C. J. Ho, Laser Ablation Synthesis of Spindle-Like Gallium Oxide Hydroxide Nanoparticles with the Presence of Cationic Cetyltrimethylammonium Bromide. J. Phys. Chem. B 108 (2004) 4940-4945.

[18] Y. Lin, Y .Liu, J. Genzer, M. D. Dickey, Shape-Transformable Liquid Metal Nanoparticles in Aqueous Solution. Chem. Sci. 8 (2017) 3832-3837.

[19] J. J. Hu, D. Xiao, X. Z. Zhang, Advances in Peptide Functionalization on Mesoporous Silica Nanoparticles for Controlled Drug Release. Small 12 (2016) 3344-3359.

[20] S. Baek, R. K. Singh, D. Khanal, K. D. Patel, E. J. Lee, K. W. Leong, et al., Smart Multifunctional Drug Delivery towards Anticancer Therapy Harmonized in Mesoporous Nanoparticles. Nanoscale 7 (2015) 14191-14216.

[21] J. G. Croissant, Y. Fatieiev, A. Almalik, N. M. Khashab, Mesoporous Silica and Organosilica Nanoparticles: Physical Chemistry, Biosafety, Delivery Strategies, and Biomedical Applications. Adv. Healthcare Mater. 7 (2018) 1700831.

[22] J. J. Hu, Q. Lei, M. Y. Peng, D. W. Zheng, Y. X. Chen, X. Z. Zhang, A Positive Feedback Strategy for Enhanced Chemotherapy Based on ROS-Triggered Self-Accelerating Drug Release Nanosystem. Biomaterials 128 (2017) 136-146.

[23] J. Zhang, Z. F. Yuan, Y. Wang, W. H. Chen, G. F. Luo, S. X. Cheng, Multifunctional Envelope-Type Mesoporous Silica Nanoparticles for Tumor-Triggered Targeting Drug Delivery. J. Am. Chem. Soc. 135 (2013) 5068-5073.

[24] Z. Y. Li, J. J. Hu, Q. Xu, S. Chen, H. Z. Jia, Y. X. Sun, A Redox-Responsive Drug Delivery System Based on RGD Containing Peptide-Capped Mesoporous Silica Nanoparticles. J. Mater. Chem. B (3) 2015, 39-44.

[25] J. Kim, C. Jo, W. G. Lim, S. Jung, Y. M. Lee, J. Lim, et al., Programmed Nanoparticle-Loaded Nanoparticles for Deep-Penetrating 3D Cancer Therapy. Adv. Mater. 30 (2018) 1707557.

[26] D. Shao, M. Li, Z. Wang, X. Zheng, Y. H. Lao, Z. Chang, et al., Bioinspired Diselenide-Bridged Mesoporous Silica Nanoparticles for Dual-Responsive Protein Delivery. Adv. Mater. 30 (2018) 1801198.

[27] Y. Lu, A. A. Aimetti, R. Langer, Z. Gu, Bioresponsive Materials. Nat. Rev. Mater. 2 (2017) 16075.

[28] Q. Tian, F. Jiang, R. Zou, Q. Liu, Z. Chen, M. Zhu, et al., Hydrophilic Cu_9S_5 Nanocrystals: A Photothermal Agent with A 25.7% Heat Conversion Efficiency for Photothermal Ablation of Cancer Cells in vivo. ACS Nano 5 (2011) 9761-9771.

[29] C. M. Hessel, V. P. Pattani, M. Rasch, M. G. Panthani, B. Koo, J. W. Tunnell, et al., Copper Selenide Nanocrystals for Photothermal Therapy. Nano Lett. 11 (2011) 2560-2566.

[30] D. K. Roper, W. Ahn, M. Hoepfner, Microscale Heat Transfer Transduced by Surface Plasmon Resonant Gold Nanoparticles. J. Phys. Chem. C 111 (2007) 3636-3641.

[31] C. Fernandez-Lopez, C. Mateo- Mateo, R. A. Alvarez-Puebla, J. Perea-Juste, I. Pastoriza-Santos, L. M. Liz-Marzan, Highly Controlled Silica Coating of PEG-Capped Metal Nanoparticles and Preparation of SERS-Encoded Particles. Langmuir 25 (2009) 13894-13899.

[32] L. Cheng; C. Wang, L. Feng, K. Yang, Z. Liu, Functional Nanomaterials for Phototherapies of Cancer. Chem. Rev. 114 (2014) 10869-10939.

[33] S. Gai, G. Yang, P. Yang, F. He, J. Lin, D. Jin, B. Xing, Recent Advances in Functional Nanomaterials for Light-Triggered Cancer Therapy. Nano Today 19 (2018) 146-187.

[34] R. Vankayala, K. C. Hwang, Near-Infrared-Light-Activatable Nanomaterial-Mediated Phototheranostic Nanomedicines: An Emerging Paradigm for Cancer Treatment. Adv. Mater. 30 (2018) 1706320.

[35] J. T. Robinson, S. M. Tabakman, Y. Liang, H. Wang, H. Sanchez Casalongue, D. Vinh and H. Dai, Ultrasmall Reduced Graphene Oxide with High Near-Infrared Absorbance for Photothermal Therapy. J. Am. Chem. Soc. 133 (2011) 6825-6831.

[36] L. Cheng, J. Liu, X. Gu, H. Gong, X. Shi, T. Liu, C. Wang, X.Wang, G. Liu, H. Xing, W. Bu, B. Sun and Z. Liu, PEGylated WS_2 Nanosheets as a Multifunctional Theranostic Agent for in vivo Dual□Modal CT/Photoacoustic Imaging Guided Photothermal Therapy. Adv. Mater. 26 (2014) 1886-1893.

[37] T. Liu, C. Wang, X. Gu, H. Gong, L. Cheng, X. Shi, L. Feng, B. Sun and Z. Liu, Adv. Mater. 26 (2014) 3433-3440.

Scheme and Figure Captions

Scheme. 1. (A) Schematic representation of the construction of immobilized liquid metal nanoparticles. After coating with silica shell, LM nanoparticles have exhibited improved colloidal stability, chemical stability and thermal stability. (B) Schematic representation of the construction of LM@MSN/DOX@HA for synergistic photothermal/chemotherapy of tumor. After targeting to tumor, overexpressed hyaluronidase (HAase) in tumor tissue could trigger the DOX release from LM@MSN/DOX@HA for chemotherapy. Simultaneously, LM@MSN was excited to produce hyperthermia under light irradiation, thus achieving highly effective synergistic photothermal/chemotherapy.

Fig. 1. (A) Schematic illustration of the preparation of LM@MSN. (B) TEM image of bare LM nanoparticles. (C) TEM images of LM@MSN with different thickness of the silica shell by varying the silica source concentrations (1.1 μM, 2.2 μM, 7.8 μM, 11.1 μM).TEM image of LM@MSN with bad control of, TEA concentrations (D_1, D_2) and stirring rate (D_3). (E) TEM image of LM@MSN treated with hydrochloric acid to etch the LM core and leave the hollow SiO_2 shell. (F) HAADF-STEM image and the corresponding element mapping of LM@MSN.

Fig. 2. (A) UV-Vis absorbance spectra of LM and LM@MSN. (B) Photothermal heating curves of LM@MSN with different concentrations under an 808 nm laser (1 W cm^{-2}) irradiation. Inset: thermal images recorded by IR camera. (C) Photothermal heating curves of LM@MSN (Ga concentration 6 μg mL^{-1}) under an 808-nm laser irradiation with different power density. Inset: thermal images recorded by IR camera. (D) Photothermal heating curves of LM@MSN or LM with different concentrations under an 808 nm laser (1 W cm^{-2}) irradiation for 10 min. (E) Photothermal effects of LM@MSN (Ga concentration 6 μg mL^{-1}) under an 808 nm laser (1 W cm^{-2}) irradiation for 10 min and then stopping the irradiation. (F) Time versus-ln(θ) plot of LM@MSN. (G) Photothermal effects of LM (Ga concentration 6 μg mL^{-1}) under an 808 nm laser (1 W cm^{-2}) irradiation for 10 min and then stopping the irradiation. (H) Time versus-ln(θ) plot of LM@MSN. (I) Thermal images of LM and LM@MSN illuminated with 808 nm laser (1 W cm^{-2})

switch-on/off for five times recorded by IR camera. (J) Photothermal heating curves of LM and LM@MSN (Ga concentration 6 μg mL^{-1}) illuminated with 808 nm laser (1 W cm^{-2}) switch-on/off for five times. (K) Time versus-ln(θ) plot of LM under second light irradiation.

Fig. 3. (A) Schematic illustration of morphology change of LM and LM@MSN after 808 nm laser irradiation for 10 min. Representative TEM images of LM (B) and LM@MSN (C) after NIR irradiation (1 W cm^{-2}) for 10 min. The hydrodynamic size (D, E), polydispersity index (PDI) (F), photographs (G) and UV-Vis absorbance spectra (H, I) of LM and LM@MSN before and after NIR irradiation (1 W cm^{-2}) for 10 min.

Fig. 4. (A) Schematic illustration of the change of LM and LM@MSN incubated in acidic solutions. Photographs (B) and variation of the absorption ratios (C) of LM and LM@MSN after incubation with different pH solutions (7.4 and 5.0) for different periods of time. Photothermal heating curves of LM (D) and LM@MSN (E) dispersed in different pH solutions for 0 h, 12 h and 24 h and illuminated with 808 nm laser (1 W cm^{-2}) for 10 min. (F) Photothermal heating curves of LM@MSN in pH 5.0 solution illuminated with 808 nm laser (1 W cm^{-2}) switch-on/off for five times.

Fig. 5. Characterization of LM@MSN/DOX@HA. (A) Schematic illustration of the preparation of LM@MSN/DOX@HA. (B) Zeta potentials of (a) LM, (b) LM@MSN, (c) LM@MSN-NH_2, (d) LM@MSN/DOX@HA. (C) Hydrodynamic size of LM@MSN/DOX@HA measured by dynamic light scattering (DLS) analysis. (D) TEM image of LM@MSN/DOX@HA. (E) Drug release profiles of DOX from LM@MSN/DOX@HA under different HAase concentrations (0, 0.15, 0.3, 0.6 mg mL^{-1}). (F) CLSM images of 4T1 cells treated with LM@MSN/DOX@HA for 2 h, 4 h, 8 h or pretreatment of free HA, respectively. Blue channel: Hoechst 33342 stained nucleus. Red channel: DOX. Scale bar: 20 μm.

Fig. 6. (A) Cell viability of 4T1 cells treated with LM@MSN@HA under 808 nm laser (1 W cm−2) irradiation for different time. (B) Cell viability of 4T1 cells treated with LM@MSN@HA under 808 nm laser irradiation for 3 min with different power density. (C, D) Cell viability of

LM@MSN@HA or LM@MSN/DOX@HA treated 4T1 cells with or without NIR irradiation (808 nm, 1 W cm−2, 3 min). Significance between every two groups was calculated was analyzed by a Student's t-test. (*p < 0.05, **p < 0.01, ***P < 0.001) (E) Corresponding fluorescence images of 4T1 cells with different conditions stained with calcein AM (green fluorescence, live cells) and PI (red fluorescence, dead cells). Scale bar: 100 μm.

Fig. 7. (A) In vivo photothermal imaging of 4T1 tumor-bearing mice after intravenously injection of LM@MSN or LM@MSN@HA and irradiated with 808 nm laser (1 W cm^{-2}) at different time point. (B) Corresponding local tumor temperature change of 4T1 tumor-bearing mice.

Fig. 8. The body weight (A) and relative tumor volume (B) of 4T1 tumor-bearing mice after various treatments for 14 days. (C) Excised tumor weight at the 14th day after various treatments. Significance between every two groups was calculated was analyzed by a Student's t-test. (***P < 0.001) (D) Photographs of representative tumor tissues at the 14th day after different treatments. (1) PBS, (2) LM@MSN@HA, (3) LM@MSN/DOX@HA, (4) LM@MSN@HA+NIR, (5) LM@MSN/DOX@HA +NIR. H&E staining images of tumor tissues (E) TUNEL immunofluorescence staining (F) and immunofluorescence staining of caspase 3 (G) after different treatments. H&E staining: 200× magnification. Scale bar: 50 μm.

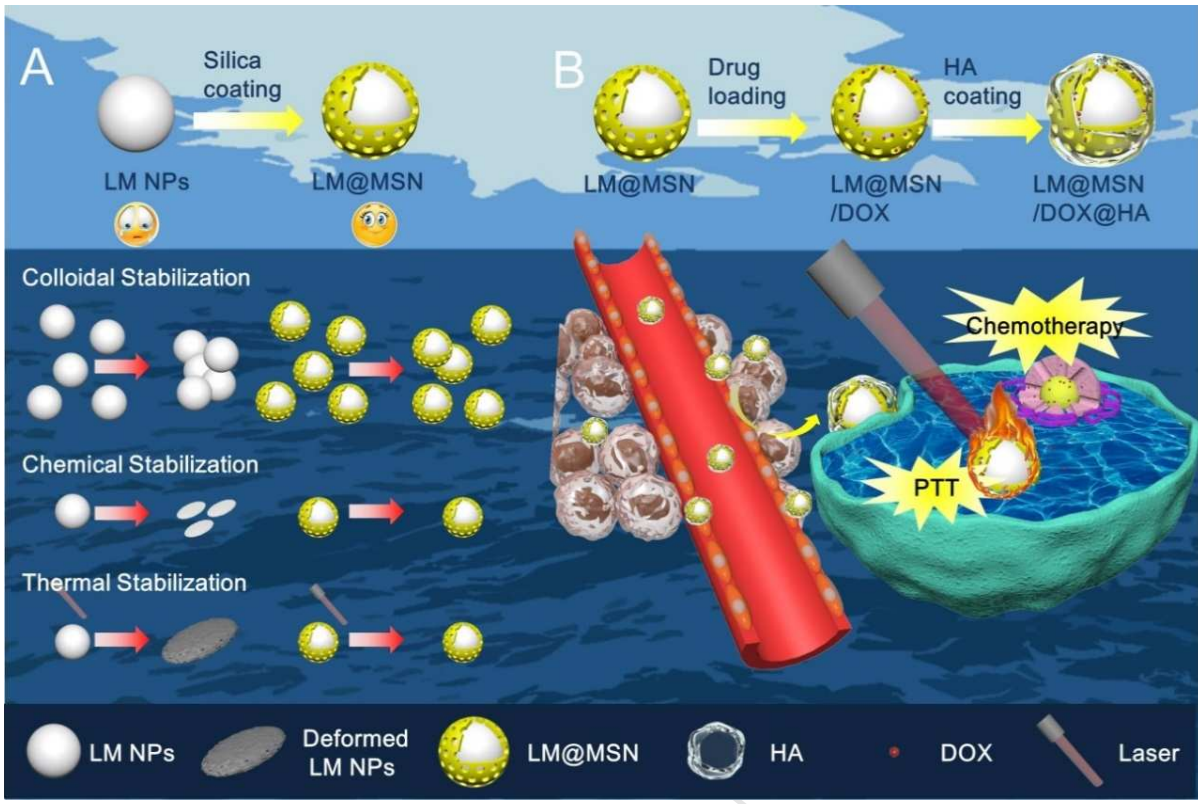

Scheme 1. (A) Schematic representation of the construction of immobilized liquid metal nanoparticles. After coating with silica shell, LM nanoparticles have exhibited improved colloidal stability, chemical stability and thermal stability. (B) Schematic representation of the construction of LM@MSN/DOX@HA for synergistic photothermal/chemotherapy of tumor. After targeting to tumor, overexpressed hyaluronidase (HAase) in tumor tissue could trigger the DOX release from LM@MSN/DOX@HA for chemotherapy. Simultaneously, LM@MSN was excited to produce hyperthermia under light irradiation, thus achieving highly effective synergistic photothermal/chemotherapy.

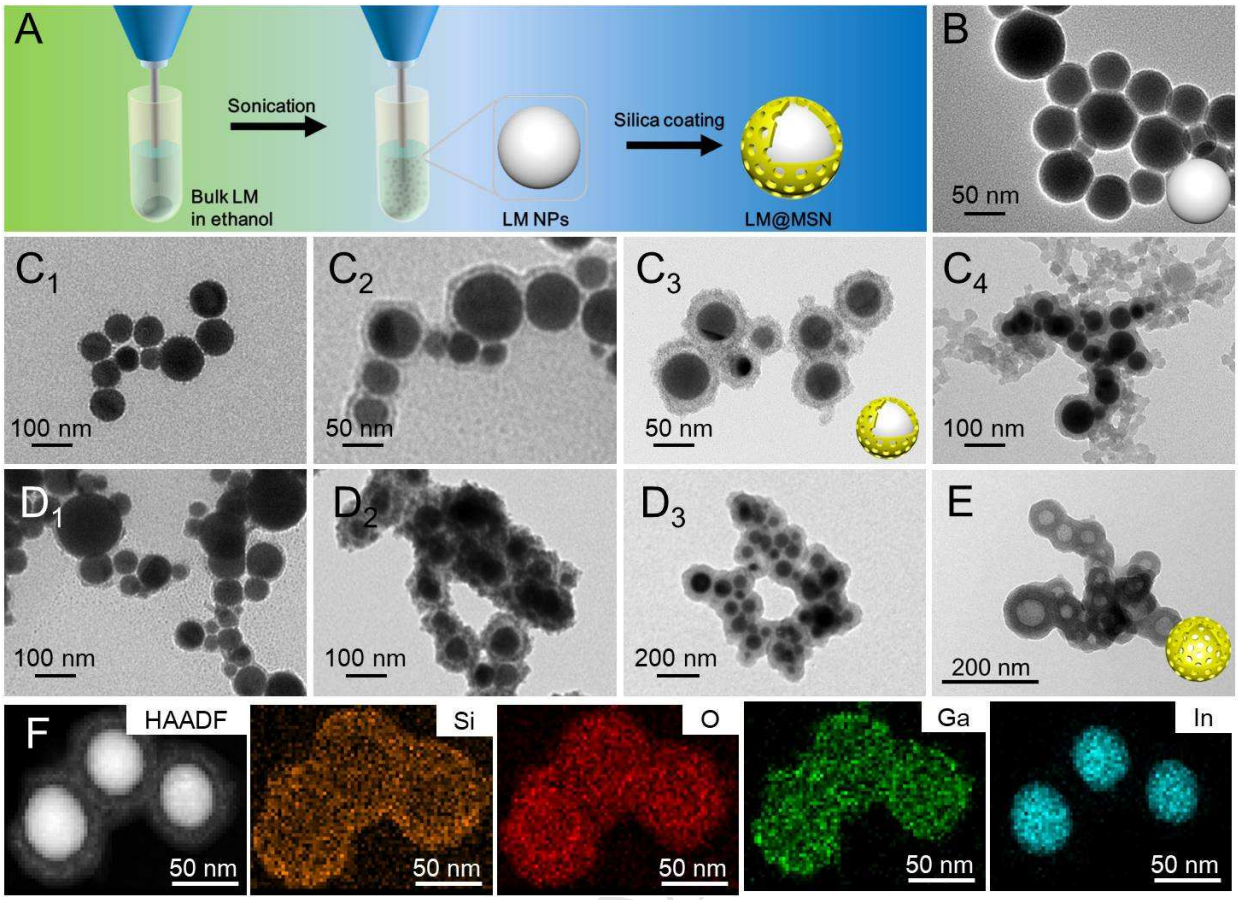

Fig. 1. (A) Schematic illustration of the preparation of LM@MSN. (B) TEM image of bare LM nanoparticles. (C) TEM images of LM@MSN with different thickness of the silica shell by varying the silica source concentrations (1.1 μM, 2.2 μM, 7.8 μM, 11.1 μM).TEM image of LM@MSN with bad control of, TEA concentrations (D_1, D_2) and stirring rate (D_3). (E) TEM image of LM@MSN treated with hydrochloric acid to etch the LM core and leave the hollow SiO_2 shell. (F) HAADF-STEM image and the corresponding element mapping of LM@MSN.

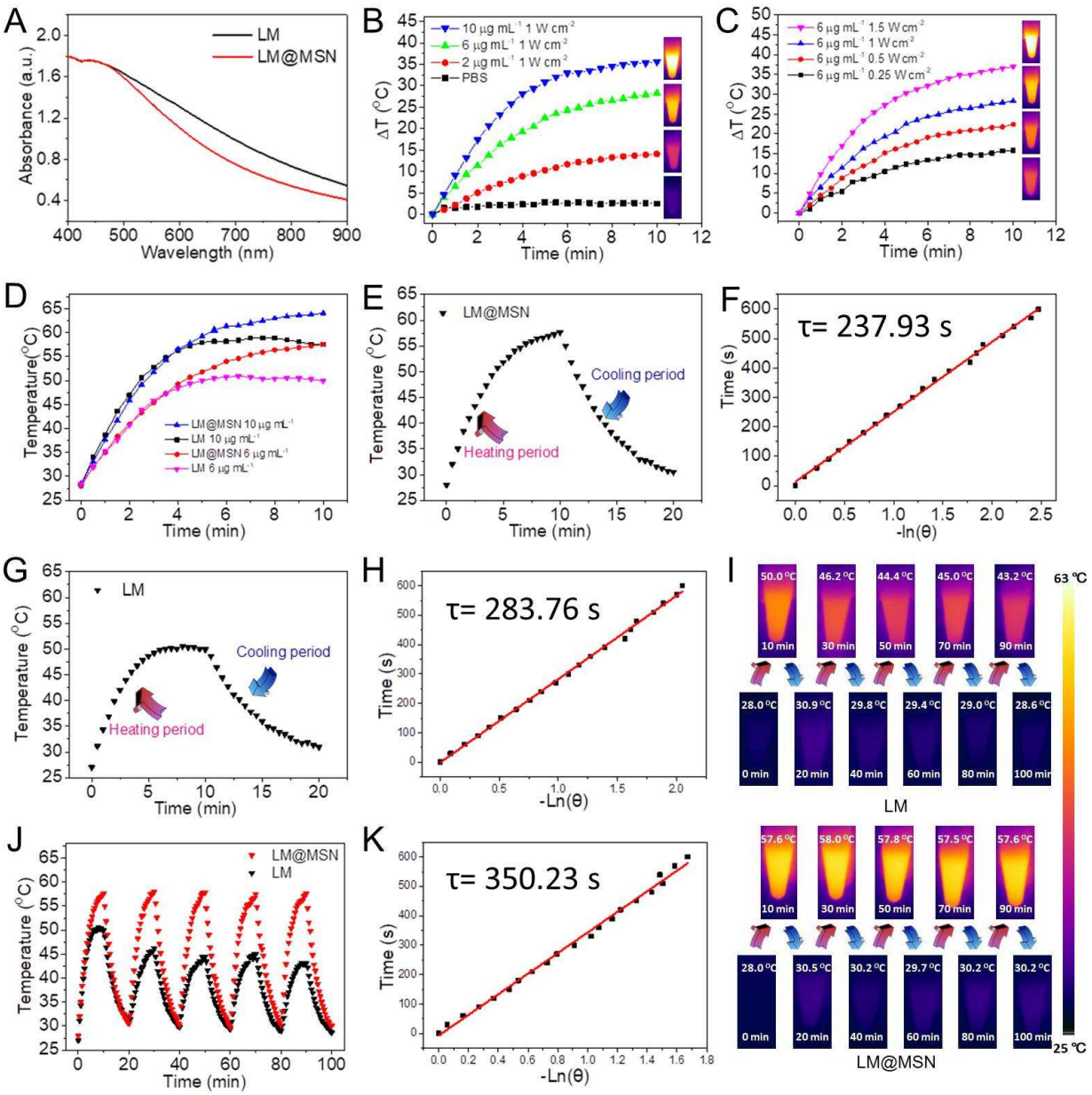

Fig. 2. (A) UV-Vis absorbance spectra of LM and LM@MSN. (B) Photothermal heating curves of LM@MSN with different concentrations under an 808 nm laser (1 W cm^{-2}) irradiation. Inset: thermal images recorded by IR camera. (C) Photothermal heating curves of LM@MSN (Ga concentration 6 μg mL^{-1}) under an 808-nm laser irradiation with different power density. Inset: thermal images recorded by IR camera. (D) Photothermal heating curves of LM@MSN or LM with different concentrations under an 808 nm laser (1 W cm^{-2}) irradiation for 10 min. (E) Photothermal effects of LM@MSN (Ga concentration 6 μg mL^{-1}) under an 808 nm laser (1 W cm^{-2}) irradiation for 10 min and then stopping the irradiation. (F) Time versus-ln(θ) plot of LM@MSN. (G) Photothermal effects

of LM (Ga concentration 6 μg mL^{-1}) under an 808 nm laser (1 W cm^{-2}) irradiation for 10 min and then stopping the irradiation. (H) Time versus-ln(θ) plot of LM@MSN. (I) Thermal images of LM and LM@MSN illuminated with 808 nm laser (1 W cm^{-2}) switch-on/off for five times recorded by IR camera. (J) Photothermal heating curves of LM and LM@MSN (Ga concentration 6 μg mL^{-1}) illuminated with 808 nm laser (1 W cm^{-2}) switch-on/off for five times. (K) Time versus-ln(θ) plot of LM under second light irradiation.

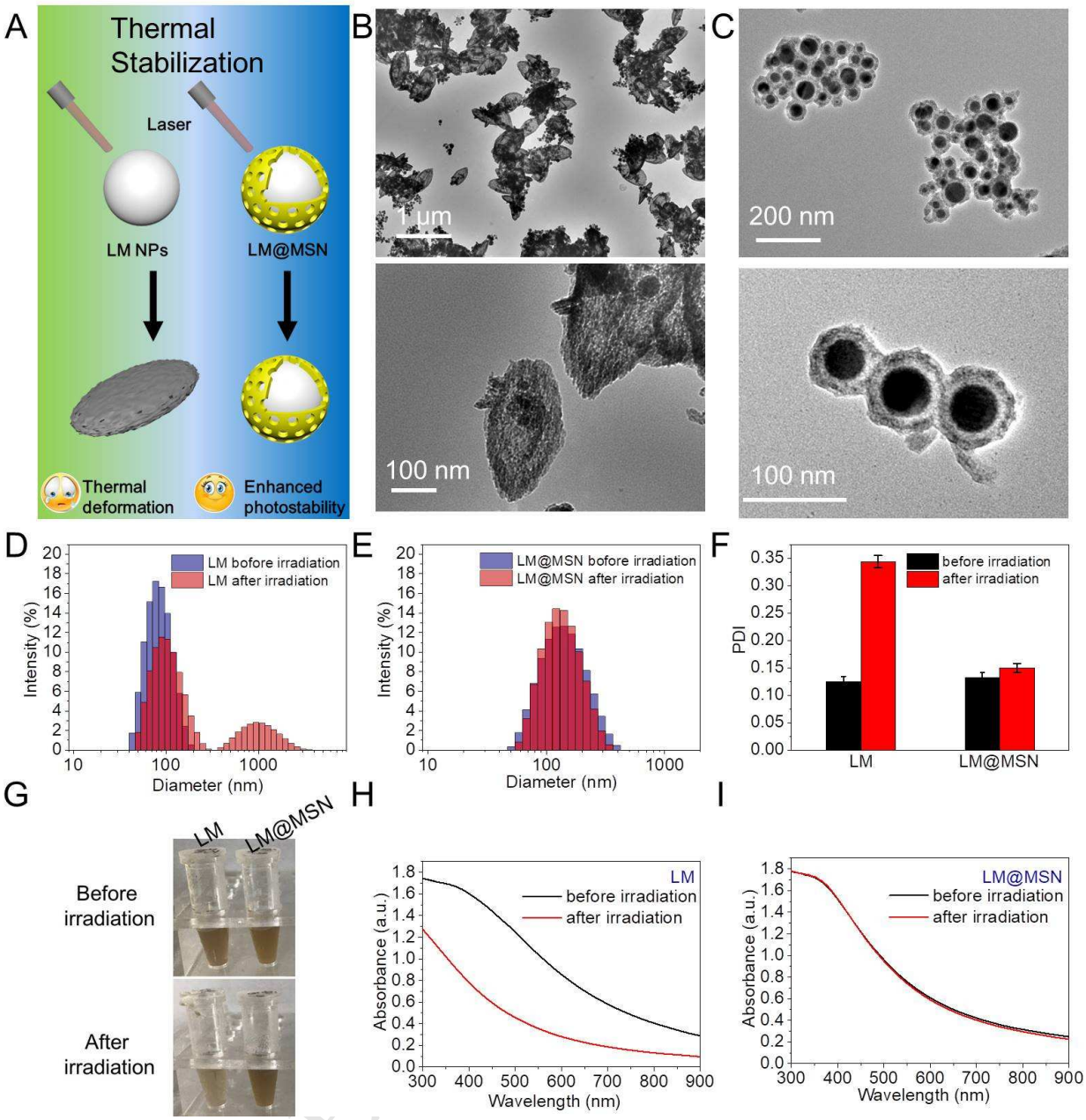

Fig. 3. (A) Schematic illustration of morphology change of LM and LM@MSN after 808 nm laser irradiation for 10 min. Representative TEM images of LM (B) and LM@MSN (C) after NIR irradiation (1 W cm^{-2}) for 10 min. The hydrodynamic size (D, E), polydispersity index (PDI) (F), photographs (G) and UV-Vis absorbance spectra (H, I) of LM and LM@MSN before and after NIR irradiation (1 W cm^{-2}) for 10 min.

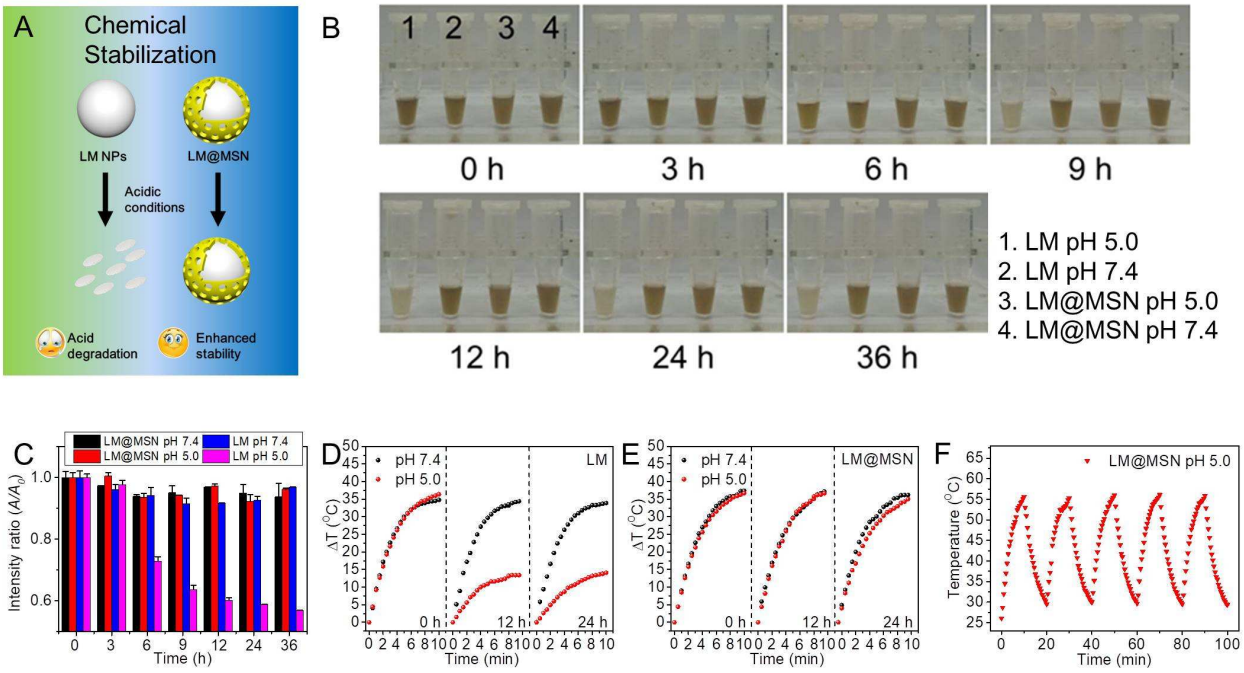

Fig. 4. (A) Schematic illustration of the change of LM and LM@MSN incubated in acidic solutions. Photographs (B) and variation of the absorption ratios (C) of LM and LM@MSN after incubation with different pH solutions (7.4 and 5.0) for different periods of time. Photothermal heating curves of LM (D) and LM@MSN (E) dispersed in different pH solutions for 0 h, 12 h and 24 h and illuminated with 808 nm laser (1 W cm^{-2}) for 10 min. (F) Photothermal heating curves of LM@MSN in pH 5.0 solution illuminated with 808 nm laser (1 W cm^{-2}) switch-on/off for five times.

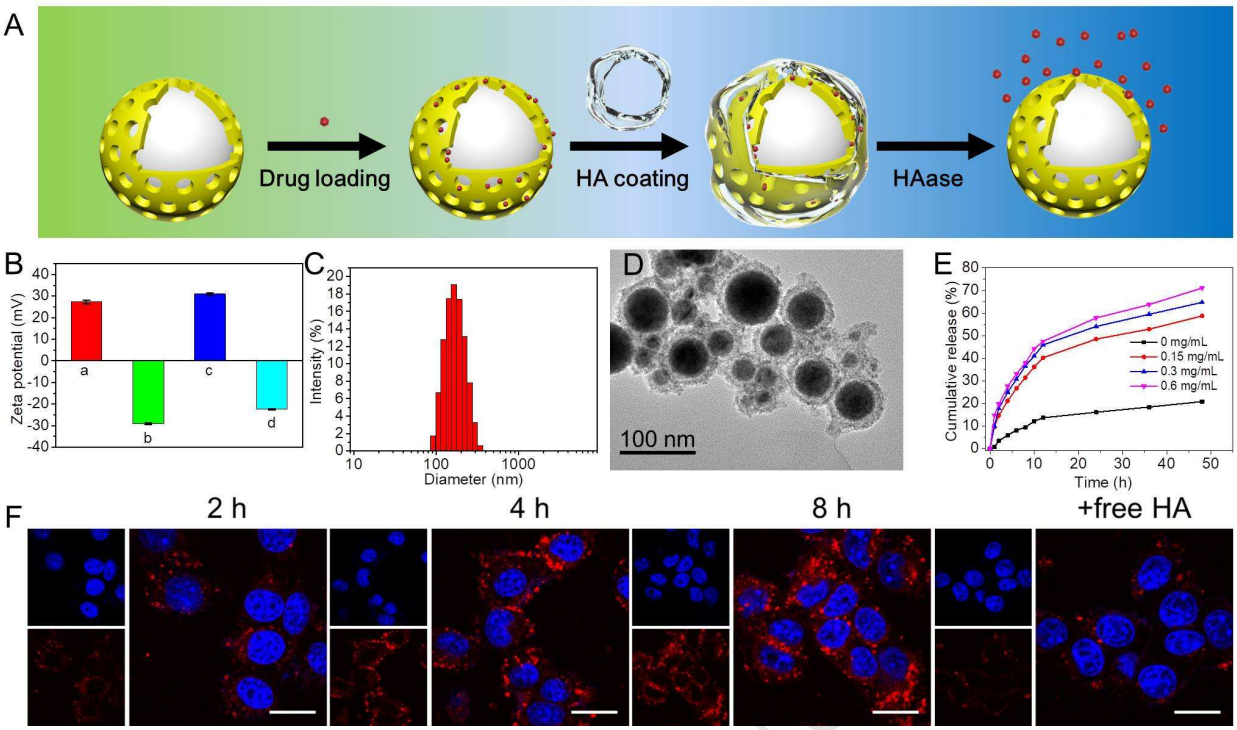

Fig. 5. Characterization of LM@MSN/DOX@HA. (A) Schematic illustration of the preparation of LM@MSN/DOX@HA. (B) Zeta potentials of (a) LM, (b) LM@MSN, (c) LM@MSN-NH_2, (d) LM@MSN/DOX@HA. (C) Hydrodynamic size of LM@MSN/DOX@HA measured by dynamic light scattering (DLS) analysis. (D) TEM image of LM@MSN/DOX@HA. (E) Drug release profiles of DOX from LM@MSN/DOX@HA under different HAase concentrations (0, 0.15, 0.3, 0.6 mg mL^{-1}). (F) CLSM images of 4T1 cells treated with LM@MSN/DOX@HA for 2 h, 4 h, 8 h or pretreatment of free HA, respectively. Blue channel: Hoechst 33342 stained nucleus. Red channel: DOX. Scale bar: 20 μm.

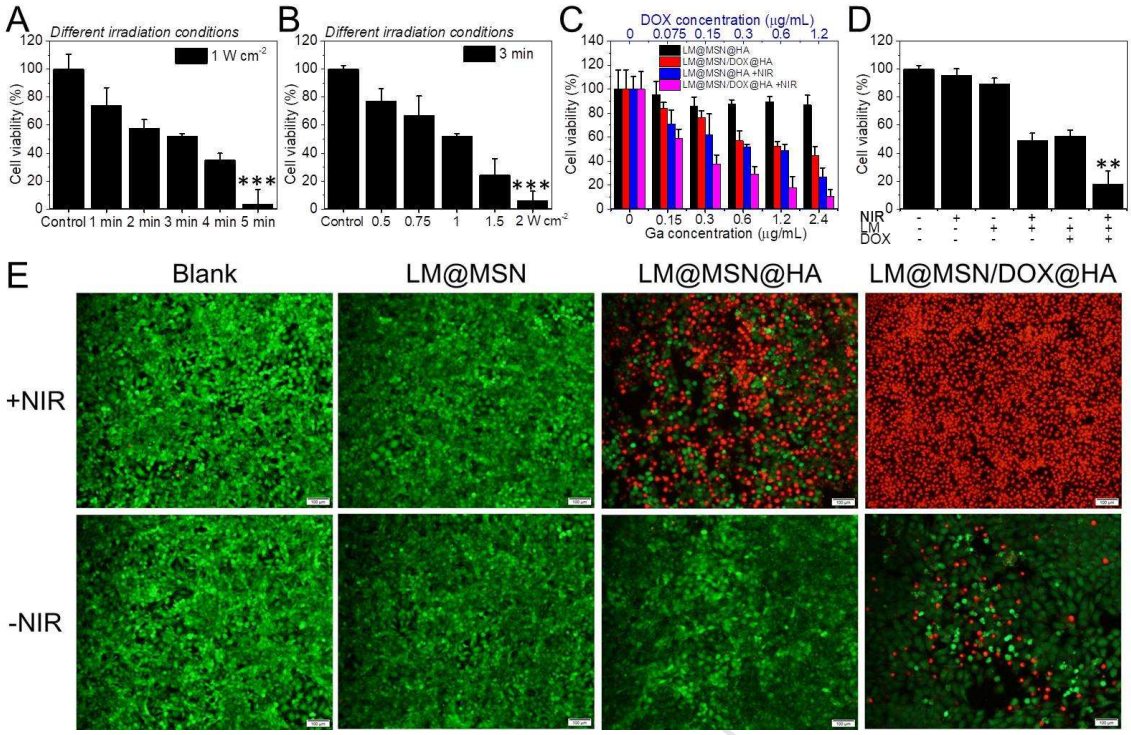

Fig. 6. (A) Cell viability of 4T1 cells treated with LM@MSN@HA under 808 nm laser (1 W cm^{-2}) irradiation for different time. (B) Cell viability of 4T1 cells treated with LM@MSN@HA under 808 nm laser irradiation for 3 min with different power density. (C, D) Cell viability of LM@MSN@HA or LM@MSN/DOX@HA treated 4T1 cells with or without NIR irradiation (808 nm, 1 W cm^{-2}, 3 min). Significance between every two groups was calculated was analyzed by a Student's t-test. (*$p < 0.05$, **$p < 0.01$, ***$P < 0.001$) (E) Corresponding fluorescence images of 4T1 cells with different conditions stained with calcein AM (green fluorescence, live cells) and PI (red fluorescence, dead cells). Scale bar: 100 μm.

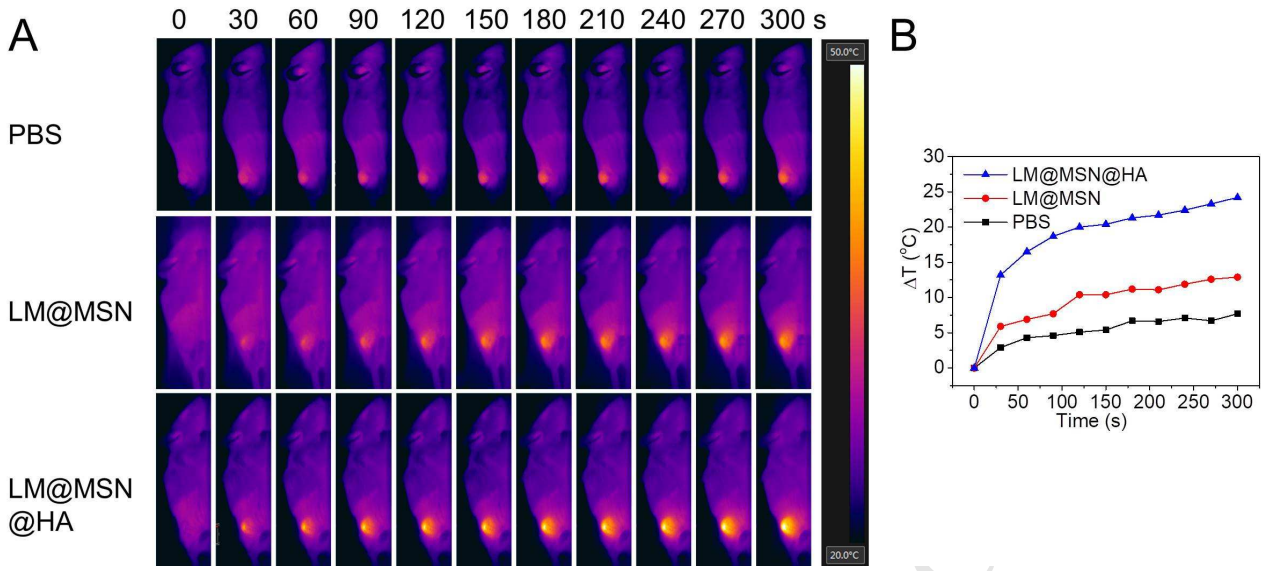

Fig. 7. (A) *In vivo* photothermal imaging of 4T1 tumor-bearing mice after intravenously injection of LM@MSN or LM@MSN@HA and irradiated with 808 nm laser (1 W cm^{-2}) at different time point. (B) Corresponding local tumor temperature change of 4T1 tumor-bearing mice.

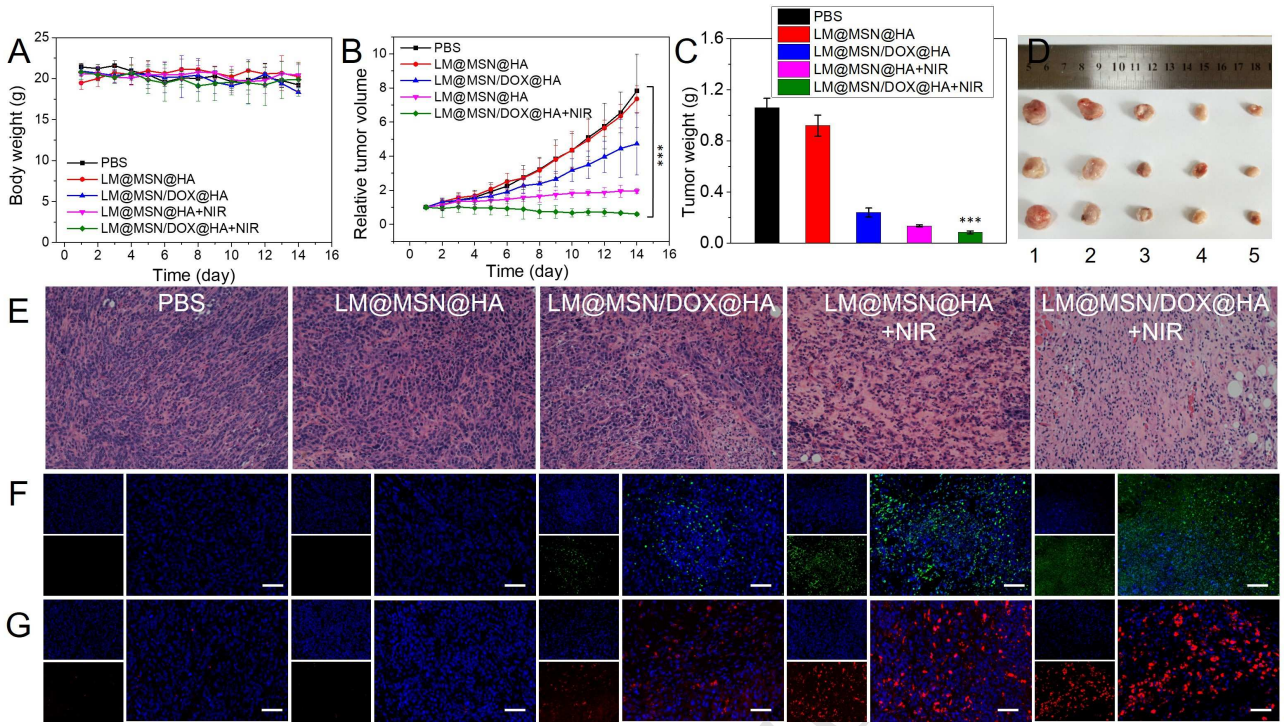

Fig. 8. The body weight (A) and relative tumor volume (B) of 4T1 tumor-bearing mice after various treatments for 14 days. (C) Excised tumor weight at the 14th day after various treatments. Significance between every two groups was calculated was analyzed by a Student's t-test. (***P < 0.001) (D) Photographs of representative tumor tissues at the 14th day after different treatments. (1) PBS, (2) LM@MSN@HA, (3) LM@MSN/DOX@HA, (4) LM@MSN@HA+NIR, (5) LM@MSN/DOX@HA+NIR. H&E staining images of tumor tissues (E) TUNEL immunofluorescence staining (F) and immunofluorescence staining of caspase 3 (G) after different treatments. H&E staining: 200× magnification. Scale bar: 50 μm.

ToC Image